Acta Geotechnica (2015) 10:1–14
DOI 10.1007/s11440-014-0363-7

RESEARCH PAPER

Instrumented nanoindentation and 3D mechanistic modeling of a shale at multiple scales

Kane C. Bennett · Lucas A. Berla · William D. Nix · Ronaldo I. Borja

Received: 17 October 2014 / Accepted: 28 November 2014 / Published online: 9 January 2015
© Springer-Verlag Berlin Heidelberg 2015

Abstract Nanoindentation tests, spanning various length scales ranging from 200 nm to 5 μm deep, were performed on a sample of organic-rich Woodford shale in both the bedding plane normal and bedding plane parallel directions. Focused ion beam milling, scanning electron microscopy, and energy dispersive X-ray spectroscopy were utilized to characterize the shale at the scale of the nanoindentation testing as being comprised predominantly of clay and other silicate minerals suspended in a mixed organic/clay matrix. The nanoindentation tests reveal the mechanical properties of the relatively homogeneous constituent materials as well as those of the highly heterogeneous composite material. Loads on the order of a few millinewtons produced shallower indents and demonstrated the elastic–plastic deformation response of the constituent materials, whereas higher loads of as much as a few hundred millinewtons produced deeper indents revealing the response of the composite matrix. In both cases, significant creep was observed. We use nonlinear finite element modeling utilizing an isotropic critical state theory with creep to capture the indentation response by calibrating plastic material parameters to the laboratory measurements. The simulations provide a means of extracting plastic material parameters from the nanoindentation measurements and reveal the capabilities as well as limitations of an isotropic model in capturing the response of an inherently anisotropic material.

K. C. Bennett · R. I. Borja (✉)
Department of Civil and Environmental Engineering, Stanford University, Stanford, CA 94305, USA
e-mail: borja@stanford.edu

L. A. Berla · W. D. Nix
Department of Materials Science and Engineering, Stanford University, Stanford, CA 94305, USA

Keywords Anisotropy · Creep · FIB-SEM · Heterogeneity · Nanoindentation · Shale

1 Introduction

Shale is a fine-grained sedimentary rock composed primarily of clay, organics, and hard minerals such as quartz, feldspar, and pyrite. It is the most common of sedimentary rocks, having been estimated to form from 44 to 56 % of all sedimentary rocks on earth [7, 34], and is of particular interest with respect to hydrocarbon production as both a source and seal rock [44, 48, 53]. Shale is found to be diverse in composition, leading to its equally diverse thermo-hydro-chemo-mechanical properties. Specifically, the type of clay and other inclusions vary among different shales, as does the presence of other constituents, such as organics, carbonates, smectite, pyrite, and other minerals [7, 29, 34].

The deformation and fracture properties of shale depend on the mechanical properties of its basic constituents. This suggests that a great deal of understanding of the overall macroscopic mechanical properties of shale (as well as other types of rocks) can be gained by studying the small-scale deformation properties of these constituents and how they upscale to the overall behavior of the composite material [4, 5, 16, 18, 52]. Furthermore, the ability to accurately model and predict a shale's stress–strain response is complicated not only by the diversity of its composition, but also by its highly anisotropic and heterogeneous nature. Most researchers agree that anisotropy of shale fabric is associated, in the most general respect, with the parallel alignment of clay particles preferentially oriented in the direction of the bedding plane, which is attributed to deposition, compaction, and/or diagenetic

processes [2, 6, 12, 20, 22–24, 31, 34, 35, 37, 38, 45, 47, 54]. Nanoscale to microscale heterogeneity is evident because shale is typically comprised of a mixture of micrometer to sub-micrometer-sized particles of clay and other minerals, often including organic material (especially when associated with hydrocarbon production) [11, 14, 15, 17, 42, 46, 49, 51, 55]. Mineral inclusions on the scale of micrometers, further, have been shown to produce inhomogeneous deformation within a surrounding clay matrix because of differential stiffness and the resulting effect on the stress field [8, 12].

This paper presents the results of nanoindentation and electron microscopy experiments on a sample of organic-rich Woodford shale, carried out for the purpose of qualitatively assessing the heterogeneity, anisotropy, and associated mechanical properties at the nanoscale to microscales. We adopt a deterministic approach to evaluating the mechanical properties of the near micrometer size particles of constituent materials, as well as the highly heterogeneous composite material. Nanoindentation testing, with indents as shallow as 200 nm deep, was used to measure in situ the deformation behavior of the relatively homogeneous regions comprised of a single material phase, while larger indentations, extending to depths as large as 5 μm, provide measurements of their composite deformation behavior. Some rocks are known to creep, particularly shales [26, 33, 43], and so all tests consisted of a peak-load hold period to measure creep. Anisotropy of material properties was evaluated by performing nanoindentation experiments in both the bedding plane normal (BPN) and bedding plane parallel (BPP) directions.

High-resolution imaging has now emerged as a viable means of describing the pore scale characteristics of heterogeneous materials at nanoscale to microscale [9, 13]. In this work, scanning electron microscopy (SEM), focused ion beam milling (FIB), and energy dispersive X-ray spectroscopy (EDX) were used in conjunction to characterize the heterogeneity and identify the constituent materials (phases) present in the indented regions. The FIB–SEM and EDX nanocharacterization provide a description of the shale sample as being comprised of near micrometer size particles of clay and other silicate minerals embedded in a mixed organic/clay matrix.

Nonlinear finite element modeling (FE) was used to simulate heterogeneous scaled nanoindentation experiments in both the BPN and BPP directions. An isotropic critical state material model with creep was employed for the simulations, which consisted (like the experiments) of large plastic strains. Drucker–Prager/Cap plasticity and consolidation creep material parameters were calibrated to the experiments as a means of evaluating plastic material properties from the nanoindentation measurements. The simulation results reveal the capabilities as well as limitations of an isotropic model in capturing the response of the inherently anisotropic shale at finite plastic strains, thus motivating the development of a finite strain anisotropic material model for shale.

2 Scale and heterogeneity

During the nanocharacterization process, a mechanistic conceptual model (a.k.a. thought model) of the nanoscale to microscale heterogeneity and fabric structure was developed based on the laboratory observations. Figure 1 shows schematically the concepts and definitions of scale so adopted with respect to heterogeneity. Three general types of constituent materials (as well as pore space) which form distinct particle grains are recognized: clay particles, other mineral particles, and organic material. We note that mica flakes are not distinguished from clay particles by EDX, and so would be classified as clay particles. The only mineral particles other than clay observed appeared to be quartz and pyrite; notably, no carbonate minerals were observed. This category, therefore, is abbreviated as QFP for quartz, feldspar, and pyrite, which are the most common silicate minerals found in shale [21, 39] and are frequently grouped together in geomechanics applications [27, 43] because they have similar material properties. Although the choice of these three broad categories of constituent materials may seem nebulous from a geochemistry point of view, they are fitting from the mechanistic point of view adopted here because they correspond to three categories encompassing the full range of constituent material stiffness: compliant (organic), medium stiffness (clay), and stiff (QFP).

The FIB–SEM imaging revealed that the shale was comprised predominantly of near micrometer size particles of these three material types; however, it was deemed necessary to define a fourth material phase: a composite of two materials, the organic/clay matrix (O/C matrix). The description of the organic/clay matrix emerged from the observation that the mineral particles and pockets of organic material did not form a supporting skeleton with inter-granular contacts, such as has been observed by some researchers [43, 46], but rather were embedded in a supporting matrix composed of varying sizes of clay plate-like shaped particles mixed with organic material, which has also been observed in organic-rich shales by other researchers [41, 49]. These plate-shaped particles of clay (mixed with organics) were observed to range down to sizes near the resolution of the SEM, i.e., with thicknesses near one nanometer. Figures 2 and 3 show the observed mineralogy and the supporting organic/clay matrix with various size plate-shaped clay particles evident. We hence

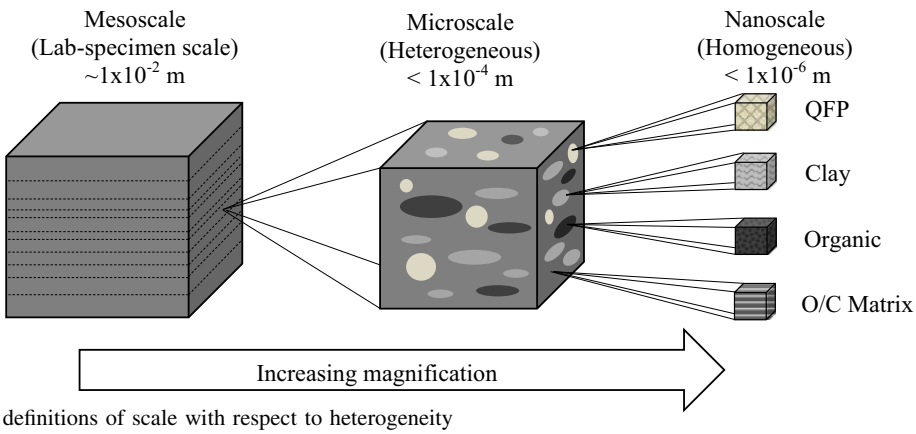

Fig. 1 Concepts and definitions of scale with respect to heterogeneity

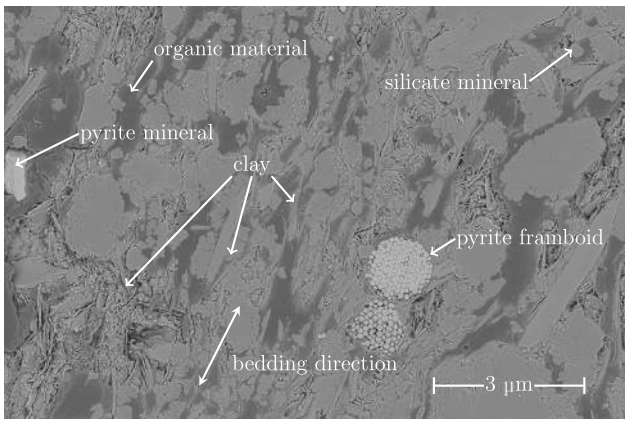

Fig. 2 SEM image of polished shale sample surface

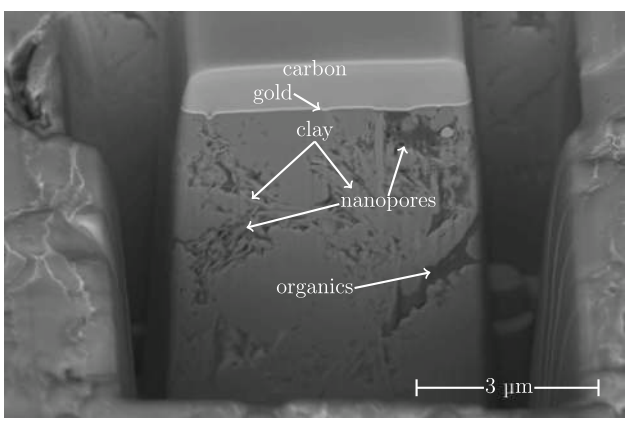

Fig. 3 SEM image of FIB milled trench into surface exposing a face for serial sectioning

make the subtle distinction between the shale being comprised of three distinct types of constituent materials, but consisting of four material phases, the fourth phase being the O/C matrix.

3 Experimental methods

3.1 Sample preparation

A sample of an organic-rich Woodford shale was obtained from a exploratory wellbore of the northern flank of the Arbuckle uplift, near the Arkoma basin, Pontotoc County, Oklahoma, USA. The samples were obtained from a depth of approximately 33–60 m, and corresponding laboratory and field characterization results can be found in [3]. The thermal maturity of the region can be estimated as oil window, between 0 and 1 % vitrinite reflectance, according to the data compiled by Cardott [10]. The samples were prepared for laboratory testing by mechanical polishing. Polishing consisted of first setting the sample in epoxy and then hand grinding two parallel faces with 400, 600, then 1,500 grit emery cloth. A Struers Labopol-5 polishing machine was then used with 6 µm diamond suspension polishing fluid, followed by 1 µm diamond suspension polishing fluid, and finally 40 nm colloidal silica suspension.

3.2 FIB–SEM and EDX methods

Focused ion beam (FIB) milling and SEM were used in conjunction (FIB–SEM) for nanocharacterization of pre- and post-indented shale specimens. The FIB–SEM nanocharacterization was performed with an FEI Helios NanoLab 600i DualBeam FIB/SEM at the Stanford Nanocharacterization Laboratory. Figure 2 shows a backscatter electron (BSE) image of a BPP shale sample. Pyrite minerals are easily distinguished by their relative brightness due to the iron they contain. Silicate minerals (particularly quartz) and clay can be more difficult to distinguish in the BSE image due to similar contrast, so they must be distinguished by shape and with aid of EDX spectroscopy. The organic matter appears very dark

because of the relatively low atomic weight of the carbon it contains. Figure 3 shows an image of a FIB milled trench cut into the shale surface. The thin coating of gold and thicker coating of carbon visible at the top of the figure are deposited to provide surface conductivity and protection from the FIB, respectively.

Energy dispersive X-ray spectroscopy (EDX) was used to identify the constituent materials present in the shale specimen. The work was performed at the Stanford Nanocharacterization Laboratory with an FEI Strata 235DB dual-beam FIB/SEM, which has element mapping and EDX microchemical analysis capability. Figure 4 shows an example EDX spectrograph of a clay particle. The spectrograph was used as an aid to identify specific shale constituents, which must otherwise be identified by their shape and contrast as detected by backscatter electron (BSE) emission.

3.3 Nanoindentation methods

Nanoindentation was performed with a diamond Berkovich tip on an Agilent Technologies Nanoindenter XP with high load capabilities. The indentation apparatus has a displacement resolution of 0.01 nm and a load resolution of 100 nN during standard loading. Nanoindentation experiments have been performed to various indentation depths, engaging the various length scales of the sample heterogeneity: 200 nm, 1, 3, and 5 μm deep. Indentations have been made into two different specimens cut from the same sample: bedding plane parallel (BPP) and bedding plane normal (BPN) oriented shale specimens. A total of 349 individual indentations were made. All were performed load (P) controlled, and displacement of the tip into the surface h was measured. The indents were made by loading to a specified indentation depth (h_{load}), with indenter loading done so as to maintain a constant indentation strain rate $\dot{P}/P$. A target effective strain rate of $\dot{P}/P = 0.05\ \mathrm{s}^{-1}$ was chosen. In all cases, the peak indentation load was held for some time to measure the creep behavior of the indented material. The peak hold time t_{creep} was 60 s for most tests, but some tests were held at peak load for as much as 20 min as extended creep tests.

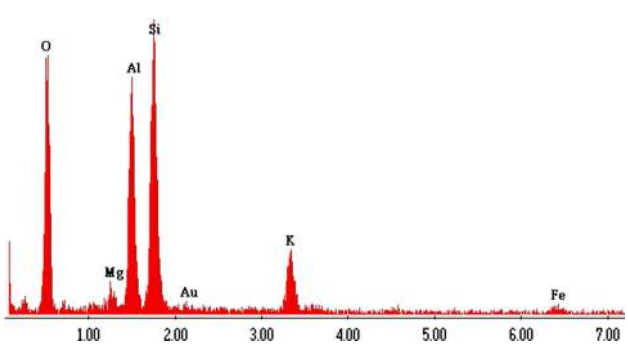

Fig. 4 Spectrograph from EDX analysis of clay particle

The nanoindentation experiments were performed in large grid patterns with known indent spacing so that individual indents could later be identified by SEM. Imaging the residual impressions with the SEM made possible identification of indents that fell on locally rough areas; data corresponding to such indents were discarded. Furthermore, with SEM, indents that were found to fall within a relatively homogeneous region comprised of a single constituent material were identified, as will be discussed in the presentation of the results in Sect. 4.2.

The material properties extracted from the nanoindentation measurements include the reduced modulus E_{r}, hardness H, and the normalized plastic work ratio W_{p}^{*}. The reduced modulus E_{r} is calculated from the initial slope of the P–h unloading curve according to

$$E_{\mathrm{r}} = \frac{1}{2\alpha}\sqrt{\frac{\pi}{A_{\mathrm{c}}}}\frac{\mathrm{d}P}{\mathrm{d}h}, \tag{1}$$

where the projected contact area A_{c} is calculated from the calibrated tip shape function, and α is a constant related to the geometry of the indenter, taken as $\alpha = 1.034$. With knowledge of the reduced modulus and Poisson's ratio ν, Young's modulus of the indented material can be found from

$$\frac{1}{E_{\mathrm{r}}} = \frac{1-\nu^2}{E} + \frac{1-\nu_i^2}{E_i}, \tag{2}$$

where E_i and ν_i are Young's modulus and Poisson's ratio, respectively, of the diamond indenter. To avoid the necessity of assuming ν, we report the effective modulus E_{s}, defined as

$$E_{\mathrm{s}} := \frac{E}{1-\nu^2}. \tag{3}$$

The hardness H is calculated as the ratio of the peak load to the projected contact area at peak load,

$$H = \frac{P_{\max}}{A_{\mathrm{c}}}. \tag{4}$$

The normalized plastic work ratio W_{p}^{*} is calculated from the areas under the loading and unloading portions of the P–h curve, which correspond to the total work W_{t} and elastic work W_{e}, respectively. The total work is assumed to be additively composed of elastic and plastic parts, i.e., $W_{\mathrm{t}} = W_{\mathrm{p}} + W_{\mathrm{e}}$, allowing for the expression of the normalized plastic work to be defined as

$$W_{\mathrm{p}}^{*} := \frac{W_{\mathrm{p}}}{W_{\mathrm{t}}} = 1 - \frac{W_{\mathrm{e}}}{W_{\mathrm{t}}}. \tag{5}$$

4 Experimental results

4.1 FIB–SEM and EDX results

FIB–SEM and EDX nanocharacterization has led to the development of the underlying thought model of heterogeneity and scales discussed in Sect. 2. The sample was observed to have a relatively high organic content compared to images reviewed in the literature. Our FIB–SEM characterization of the shale sample provides a description of the shale at this scale as being comprised of near micrometer sized particles of clay and other silicate minerals embedded in a mixed organic/clay matrix. Nearly everywhere that organic material is observed, clay platelets are found to be interspersed within, as seen in Figs. 2 and 3.

The SEM imaging was also instrumental in evaluating the local surface roughness and constituent materials present at the location of the indentations, as is discussed next in the Sect. 4.2. Figure 5 shows a backscatter electron (BSE) image of the residual impression left by a 3 μm deep BPP indentation into a highly heterogeneous region.

4.2 Nanoindentation results

Each indentation locus from the full set of BPN and BPP nanoindentation results were examined individually by SEM in order to (1) disregard indents that fell on a locally rough surface and (2) identify indents which fell on relatively homogeneous regions comprised of a single constituent material. It is well known that surface roughness can lead to inaccuracy in indentation measurements [32], and, therefore, it is important to ensure that indentation measurements are performed on an adequately smooth surface. This can prove to be a challenge in the case of shale because of its highly heterogeneous nature at the scale of the nanoindentation testing. It was thus decided that each indentation locus would be examined individually by SEM so that the local surface roughness could be evaluated and those that fell on locally rough surfaces discarded. Examination of the surface engaged by each indentation measurement, furthermore, allowed the material comprising the surface at the location of the indent to be evaluated. Because the heterogeneity at the scale of the indents consisted of approximately micrometer size particles of clay and silicate mineral grains suspended in a mixed organic/clay matrix, some of the 200 nm deep indentations were found to engage, at least predominantly, a single material phase. The 1 μm deep indentations were found to be generally too large to fall within a single homogeneous phase; however, some of them were found to fall *between* particles, i.e., in regions comprised of only the organic/clay matrix, and some were found to fall in relatively large pockets of organic material. Indentations 3 μm deep and larger were found to fall in heterogeneous regions, with the exception of two of the 3 μm deep indentations which fell within (relatively) large pockets of organic material.

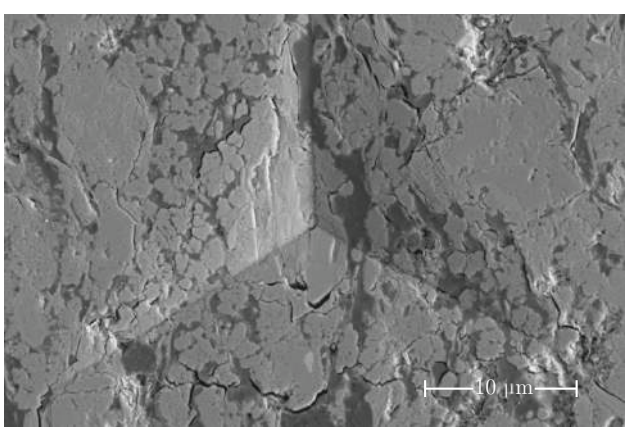

Fig. 5 Backscatter electron (BSE) image of post-indented region of 3 μm deep BPP test showing residual impression within highly heterogeneous material

The 200 nm deep indents are thus divided into three groups: those that fell on particles of clay, those that fell on other silicate mineral particles (abbreviated QFP) and those that fell on regions of organic matter. It should be noted that while some of the 200 nm deep indentations were found to fall on predominantly a single phase, surrounding constituent materials and the supporting matrix likely influence to some extent the indentation measurements. Figure 6 presents nanoindentation load-displacement curves obtained from 200 nm deep indents, with the results grouped as described above. Table 1 shows the subsequently extracted mechanical properties. The 1 μm deep indentations provide measurements of the mechanical properties of the O/C matrix, reported in Table 2.

Other than the previously mentioned two which fell in relatively large pockets of organic material, the indentations to depths of 3 μm were found to fall on heterogeneous regions, as were all of the 5 μm deep indentations. Figure 7 shows how the 5 μm deep indentations varied relatively little, being representative of the deformation behavior of the composite (heterogeneous) material. The extracted mechanical properties for the heterogeneous material at these scales are presented in Table 3, and extracted mechanical properties of the organic material are presented in Table 4.

4.3 Discussion of experimental results

Shallower indentations on the order of 200 nm into individual particle grains reveal a distinct difference between the constituent materials with respect to strength and

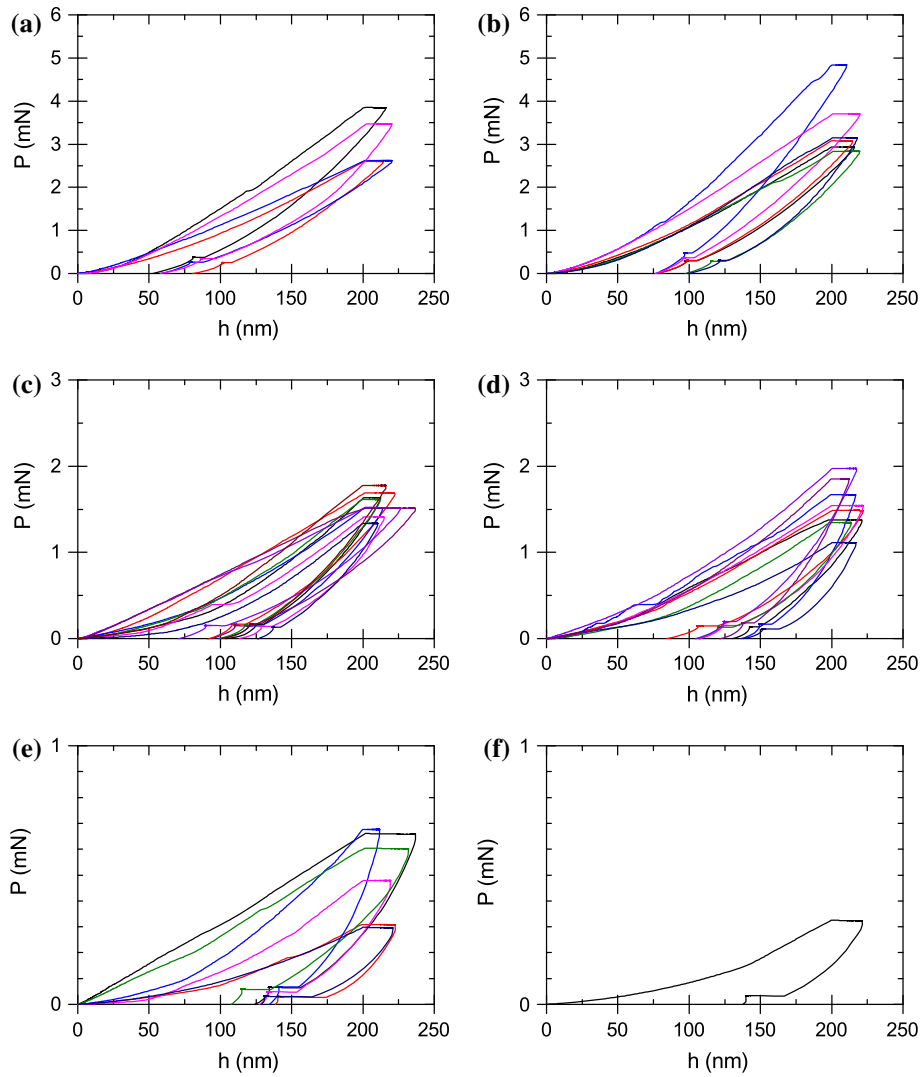

Fig. 6 BPN (*left*) and BPP (*right*) load-versus-displacement curves for 200 nm deep indentations grouped by the constituent material on which they fell, **a** BPN indentations into QFP-silicate mineral grains, **b** BPP indentations into QFP-silicate mineral grains, **c** BPN indentations into clay particles, **d** BPP indentations into clay particles, **e** BPN indentations into organic material, **f** BPP indentation that fell on pocket of organic material

stiffness, evaluated on the basis of the extracted material properties of Table 1. For example, the QFP-silicate minerals exhibit by far the highest strength and stiffness in terms of E_s, H and W_p^*, which can also be inferred from the intensity of load P generated for a given indentation of 200 nm as seen in Fig. 6. Clay particles exhibit lower strength and stiffness, followed by the organics, which are clearly the weakest and most compliant of the constituent materials. The stiffest particle grains (the QFP-silicate minerals) are approximately five times as stiff as the most compliant (organic) material, evaluated by E_s, and the hardness H varies by approximately an order of magnitude between these two constituent materials. The plastic work ratio W_p^* does not vary as much between constituents, but does show that indentations that fell on QFP-silicate mineral grains consisted of significantly less relative plastic work than the those that fell on clay and organic regions. We note that this increase in W_p^* corresponds to either an increase in ductile plastic flow or nanoindentation induced fracture—or some combination thereof, and that some researchers have suggested that W_p^* may be indicative of the propensity for fracture in shales [19].

As a means of quantifying the degree of anisotropy exhibited with respect to BPN and BPP indentation measurements at a specific indentation depth, we define the anisotropy ratio $K_{(\cdot)}$ as the ratio of an extracted material property from BPP and BPN indentation directions, i.e.,

$$K_{(\cdot)} := \frac{(\cdot)_{\mathrm{BPP}}}{(\cdot)_{\mathrm{BPN}}}, \tag{6}$$

Table 1 Measured mechanical properties of each of the constituent materials as measured by 200 nm deep indentation tests in both BPN and BPP orientations, corresponding to Fig. 6

	BPN			BPP		
	Mean	SD	COV (%)	Mean	SD	COV (%)
QFP						
E_s (GPa)	32.750	7.287	22.25	38.114	7.029	18.43
H (GPa)	4.515	0.713	15.79	4.815	1.502	31.19
W_p^*(%)	50.59	1.84	3.64	55.92	4.73	8.46
Clay						
E_s (GPa)	20.373	2.927	14.37	25.865	5.692	22.01
H (GPa)	1.801	0.242	13.42	1.592	0.332	20.83
W_p^*(%)	61.02	2.24	3.67	68.93	5.45	7.91
Organic						
E_s (GPa)	8.780	3.094	35.24	6.503	–	–
H (GPa)	0.449	0.155	34.60	0.278	–	–
W_p^*(%)	62.32	24.52	39.35	74.61	–	–

Table 2 Measured mechanical properties of organic/clay matrix as measured by 1 μm deep indentation tests in both BPN and BPP orientations

	BPN			BPP		
	Mean	SD	COV (%)	Mean	SD	COV (%)
O/C matrix						
E_s (GPa)	12.392	1.498	12.09	18.545	1.975	10.65
H (GPa)	0.604	0.075	12.38	0.592	0.088	14.81
W_p^*(%)	67.98	2.78	4.09	74.69	3.24	4.34

where $(\cdot)$ is the material property determined from either BPN or BPP indentation tests. For example, the anisotropy ratio of hardness is written as $K_H = H_{BPP}/H_{BPN}$. In Table 5, we report $K_{(\cdot)}$ for various material phases as determined from the shallower indentations. Notably, the O/C matrix exhibits strong elastic anisotropy, with about a 50 % increase of stiffness in the BPP indentation direction. The clay phase similarly exhibits strong stiffness anisotropy, about a 27 % increase in BPP direction, and even the QFP-silicate minerals exhibit in situ about a 16 % increase in stiffness in the BPP direction. We emphasize, however, that although these shallow indentations are within regions comprised of a single material phase, the surrounding and underlying materials may include other phases, such as the O/C matrix, for example, which may influence the measurements to some degree. The relative amount of plastic work W_p^* appears to be consistently about 10 % or so greater in the BPP direction for QFP, clay and O/C matrix phases. While the hardness of the O/C matrix is nearly the same for BPN and BPP indentation directions and the QFP phase exhibits only a slight increase in the BPP direction, the clay phase hardness is, interestingly, significantly less in the BPP direction. We hypothesize that this may be attributable to the parallel alignment of plate-like clay particles, as also may be the increased stiffness in this direction. For example, it may be attributed to BPN deformations including significant bending of plate-like particles in addition to bulk deformation, whereas bending deformation in the BPP direction is much less, and there could also be preferential slip and microfracture occurring along the plate-like surfaces (hence occurring preferentially in the bedding plane direction)—further research is needed to explain with confidence the mechanisms behind the observed anisotropy in these measurements.

It is very likely that the indentation response for at least some of the organic material indents has been influenced to a significant extent by the presence of underlying stiffer materials that were not detected by SEM imaging of the post-indented surface. This may explain the non-uniformity of the BPN 200 nm deep indentations into organic material

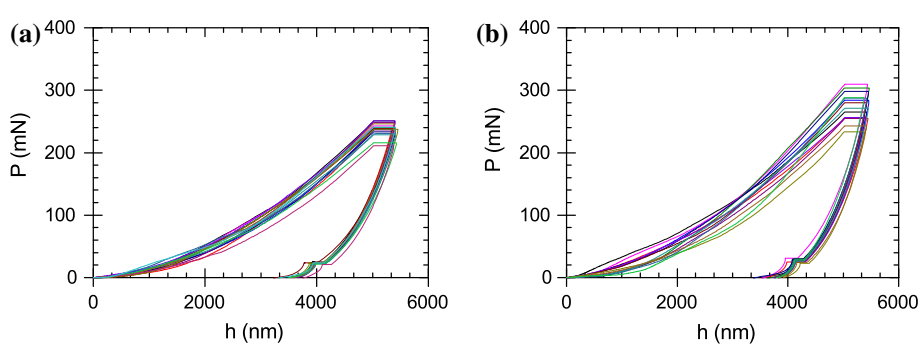

Fig. 7 BPN (*Left*) and BPP (*Right*) 5 μm deep indentations into heterogeneous regions showing repeatability of measurements, indicating that they are representative of the composite material response, **a** BPN heterogeneous, **b** BPP heterogeneous

Table 3 Measured mechanical properties of heterogeneous shale measured at various length scales in both BPN and BPP orientations

Depth (μm)	BPN			BPP		
	Mean	SD	COV (%)	Mean	SD	COV (%)
3						
E_s (GPa)	12.981	0.554	4.27	17.187	1.174	6.83
H (GPa)	0.480	0.041	8.48	0.556	0.073	13.20
W_p^*(%)	71.75	1.64	2.29	75.53	19.54	25.87
5						
E_s (GPa)	11.792	0.622	5.28	15.174	0.763	5.02
H (GPa)	0.406	0.020	4.99	0.452	0.038	8.52
W_p^*(%)	72.95	1.04	1.43	76.51	1.51	1.97

Table 4 Measured mechanical properties of organic material measured at various length scales and in both BPN and BPP orientations

Depth (μm)	BPN			BPP		
	Mean	SD	COV (%)	Mean	SD	COV (%)
1						
E_s (GPa)	10.668	1.124	10.53	9.511	1.573	16.53
H (GPa)	0.295	0.041	14.14	0.299	0.097	32.44
W_p^*(%)	78.07	2.81	3.60	72.52	2.28	3.14
3						
E_s (GPa)	6.173	–	–	10.042	–	–
H (GPa)	0.282	–	–	0.317	–	–
W_p^*(%)	60.42	–	–	70.35	-	–

Table 5 Anisotropy ratio $K_{(\cdot)}$ of constituent materials as measured by 200 nm and 1 μm deep indentations

Depth	Phase	K_E	K_H	$K_{W_p^*}$
200 nm	QFP	1.16	1.07	1.11
	Clay	1.27	0.88	1.13
1 μm	O/C matrix	1.50	0.98	1.10

Table 6 Anisotropy ratio $K_{(\cdot)}$ of composite (heterogeneous) shale, as measured at greater indentation depths

Depth (μm)	Phase	K_E	K_H	$K_{W_p^*}$
3	Composite	1.32	1.15	1.05
5	Composite	1.29	1.11	1.05

exhibited in Fig. 6. The lenticular shape of the pockets of organic material (see Fig. 1) provides a possible explanation for both the lack of uniformity in BPN measurements (due to stiffer materials underlying relatively shallow pockets of organics) and also the relative dearth of BPP indentations that fell exclusively on organic material (due to the thinner vein-like shape of the BPP exposed pockets of organic material making it difficult for an indentation to fall sufficiently far from an edge to be considered within a single phase).

Deeper indentations on the order of 3–5 μm produced much more consistent and reproducible indentation measurements, as is evident in Fig. 7. For indentations of this depth, a highly heterogeneous region of the shale is expected to have been engaged, and the results are less susceptible to local variations of constituent mechanical properties. The reproducibility of indentations performed at this scale, further, suggests that these measurements are sufficiently large to be representative of the composite stress strain behavior of the heterogeneous shale at the microscale of Fig. 1. Table 6 shows that there is also strong evidence of anisotropy exhibited at this scale, with the strength and stiffness consistently being higher in the BPP than in the BPN directions. We note that this may also be due to the parallel alignment of clay particles within the O/C matrix.

Creep responses are quite significant not only for the composite heterogeneous shale, but also for each of the material phases, including the much harder QFP-silicate minerals. It is very likely that even the shallower, 200 nm

deep, indentations have produced so-called 'pressure bulbs' that triggered creep on underlying organics and clay materials, since even the harder QFP-silicate minerals (supported by these softer materials) appear to have developed significant creep deformation. We might expect this kind of interaction between constituent materials when performing in situ force-displacement measurements, making the measurement of individual constituent mechanical properties challenging.

5 FE model

5.1 Model development

The FE model was developed for the purpose of assessing the degree of anisotropy pending the development of a truly anisotropic model as part of ongoing research efforts. It is, therefore, not meant to act as a surrogate to an anisotropic model, but rather, is intended to gage how far an isotropic model falls short in describing the anisotropic behavior of the shale exhibited in the nanoindentation experiments. To this end, we modeled BPN and BPP 3 μm deep indentations, calibrating the material parameters separately to the average values obtained from each set of experiments. In this way, plastic material parameters were obtained, corresponding to both the BPN and BPP nanoindentation measurements.

Figure 8 shows the meshed nanoindentation model with a Berkovich indenter tip, consisting of a total of 10,161 elements. The nonlinear FE modeling was done in Abaqus/standard with implicit integration. The shale was modeled with linear hexahedral elements using full integration, and the Berkovich tip was modeled as a rigid body (its motion governed by a reference node at its tip) with a mixture of linear quadrilateral and linear triangular elements. The contact between shale and the indenter was modeled as surface-to-surface frictionless contact with a finite-sliding Lagrange multiplier formulation. The boundary conditions (BC's) of the shale were prescribed as fully fixed (essential BC's) at the base, laterally fixed at the sides, and fully free (natural BC's) at the top surface where the indenter made contact.

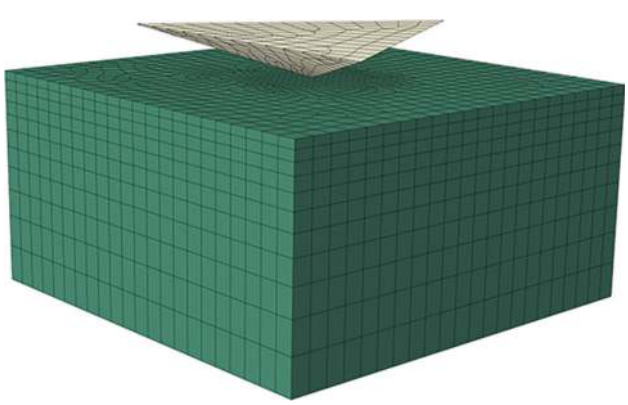

Fig. 8 Meshed model of shale nanoindentation with a Berkovich indenter tip

Both the BPN and BPP 3 μm deep heterogeneous indentations were simulated. Imitating the nanoindentation experiments, the simulations were performed to a specified indentation depth h by controlling the applied load P so as to maintain a constant indentation rate (see Sect. 3.3). That is, during simulated loading, the load was made to evolve over time according to

$$P(t) = P_0 e^{kt}. \tag{7}$$

The loading parameters P_0 and k were determined from the experiments to be 0.022 mN and 0.0156 s^{-1}, respectively. Once the target depth was reached, the load was held constant for 60 s, and then the indenter was unloaded (linearly in time) to $P = 0$ over 20 s.

Because the nanoindentation experiments show significant creep in addition to plastic deformation, a viscoplastic creep material model has been pursued. Specifically, isotropic linear elasticity and a Modified Drucker–Prager/Cap plasticity with consolidation hardening and creep were chosen. Modified Drucker–Prager/Cap plasticity is based on the well known Drucker–Prager plasticity yield criterion for granular materials [30] with the addition of a cap bounding the yield surface in the direction of the mean normal stress p (along the hydrostatic axis). A detailed description of the material model can be found in [1] and is not repeated here; however, a general description and definition of the material parameters is provided in what follows.

Denoting tensors in boldface, we note the use of $\mathbf{1}$ for the second order identity tensor and $\boldsymbol{\sigma}$ for the Cauchy stress tensor. The inner (scalar) product of two tensors is signified by the double dot, e.g., $\boldsymbol{A} : \boldsymbol{B} = \mathrm{tr}[\boldsymbol{A}^T\boldsymbol{B}]$, where we have denoted the matrix transpose with the superscript T and the matrix trace operator $\mathrm{tr}[\,\cdot\,]$. The deviatoric stress $\boldsymbol{S}$ is given by $\boldsymbol{S} := \boldsymbol{\sigma} - 1/3\mathrm{tr}[\boldsymbol{\sigma}]\mathbf{1}$.

The yield surface is defined in p-q space, where the mean normal stress p and Mises equivalent stress q are defined as

$$p := \frac{1}{3}\mathrm{tr}[\boldsymbol{\sigma}], \quad q := \sqrt{\frac{3}{2}\boldsymbol{S} : \boldsymbol{S}}. \tag{8}$$

The cohesion d and the friction angle β define the cohesive bounding surface (in the direction of q). The creep formulation is restricted to an associated flow rule (no dependence on the third stress invariant). The initial intersection of the cap with the hydrostatic axis $p_{b(1)}$ is

specified along with a second hydrostatic yield stress point $p_{b(2)}$ and a corresponding amount of plastic volumetric strain $\varepsilon_v^{\mathrm{pl}}$, which together define linear cap hardening.

The total strain $\boldsymbol{\varepsilon}$ is assumed to be additively composed of elastic and inelastic (plastic) parts, with the inelastic strain, furthermore, composed of the time-independent part $\boldsymbol{\varepsilon}^{\mathrm{pl}}$ and the time-dependent (creep) part $\boldsymbol{\varepsilon}^{\mathrm{cr}}$, such that

$$\boldsymbol{\varepsilon} = \boldsymbol{\varepsilon}^{\mathrm{el}} + \boldsymbol{\varepsilon}^{\mathrm{pl}} + \boldsymbol{\varepsilon}^{\mathrm{cr}}. \tag{9}$$

The creep is defined with respect to the mean normal stress p (consolidation creep), where the effective creep pressure $\bar{p}^{\mathrm{cr}}$ describes a pressure within the yield surface but greater than a threshold creeping pressure (explicitly related to the yield surface cap position). The creep strain increment $\Delta\boldsymbol{\varepsilon}^{\mathrm{cr}}$ is proportional to the equivalent creep strain $\bar{\varepsilon}_c^{\mathrm{cr}}$, which is determined from a uniaxial consolidation law. A time (t) dependent uniaxial creep law was chosen, given by

$$\dot{\bar{\varepsilon}}_c^{\mathrm{cr}} = A(\bar{p}^{\mathrm{cr}})^n t^m, \tag{10}$$

where A, n, and m are material parameters.

5.2 Simulation results and discussion

Calibration of material model parameters was performed separately for the bedding plane normal (BPN) and bedding plane perpendicular (BPP) indentation tests. Initial trial material model parameters were estimated from the nanoindentation results (Sect. 4.2) along with consideration of other published laboratory testing results [3, 28, 36, 43]; however, the final material model parameters were determined by calibrating the P–h curves resulting from the simulated nanoindentation tests with the measurements obtained from the nanoindentation experiments.

A single average P–h measurement curve was established separately for both the BPN and BPP 3 μm data sets. These mean-measurement curves were established as having the mean peak load $\bar{P}_{\max}$ and amount of creep during the peak-load hold period $\Delta\bar{h}_{\mathrm{creep}}$ corresponding to the respective set of measurements (BPN and BPP). The average loading and unloading portion of the mean-measurement curves were then determined separately by least squares polynomial regression for each of the BPN and BPP data sets.

Figure 9 presents the results of the BPN and BPP calibrated nanoindentation simulations alongside the corresponding mean-measurement curve to which they were calibrated. We emphasize these simulation results are for an isotropic material model calibrated separately to the BPN and BPP laboratory measurements. Calibration with each of the mean-measurement curves began with trying to match the average Young's modulus extracted from the corresponding indentation measurements and assuming a

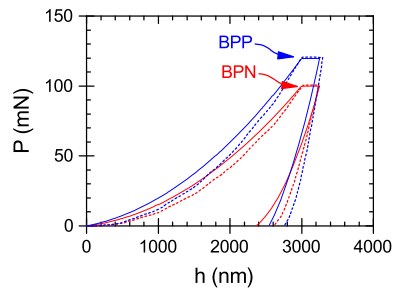

Fig. 9 BPN and BPP simulation results compared with corresponding averaged curve from laboratory measurements. Measurements are shown with *solid lines* and simulations with *dashed lines*

Poisson's ratio of $\nu = 0.3$; however, it was found that those values needed to be lowered in order to reproduce the measured P–h curves. This may be due at least in part, as has been suggested by some authors (e.g., [40]), to the effect of the indenter tip geometry in relation to its area in contact with the shale surface at any given depth h: The Berkovich tip was modeled as ideally shaped, i.e., a three-sided pyramid coming to a perfect point, whereas the reduced modulus calculated according to Eq. 1 from the measurements assumes the contact surface corresponds to the impression left from an elliptic paraboloid described by the tip shape function A_c. It was, therefore, decided to reduce the Young's moduli for both BPN and BPP simulations to those needed to best match the mean-measurement curves, but to maintain the same anisotropy ratio $K_{\mathrm{E}} = 1.32$ between BPP and BPN simulations as that determined from the measurements. The plastic (including plastic creep) material model parameters were then calibrated for BPN and BPP simulations to best match the corresponding average measurement curves. Only the Drucker–Prager/Cap plasticity model parameters d, β, and $p_{b(1)}$, defining the yield surface in p-q space, were taken as anisotropic. The change in hydrostatic pressure $\Delta p_b = p_{b(2)} - p_{b(1)}$ as well as the corresponding amount of volumetric strain $\varepsilon_v^{\mathrm{pl}}$, defining linear hardening, were taken as isotropic. Notably, the creep parameters were able to be taken as isotropic and still match reasonably well both BPN and BPP mean-measurement curves, although the creep potential surface itself is defined relative to the yield surface (Sect. 5.1) and is, therefore, anisotropic. All of the calibrated material model parameters are presented in Tables 7 and 8 for the BPN and BPP simulations, respectively.

The disparity between the two sets of curves (BPN and BPP) in Fig. 9 and the two sets of calibrated material parameters in Tables 7 and 8 is indicative of the material anisotropy. Anisotropy ratios determined from the calibrated material model parameters are presented in Table 9. Interestingly, all three of the calibrated plastic anisotropy

Table 7 Calibrated material model parameters for BPN simulation

E (GPa)	Drucker–Prager plastic			Cap hardening		Creep consolidation		
	ν	d (MPa)	β	$p_{b(1\&2)}$ (MPa)	ε_v^{pl}	A ($Pa^{-n}s^{-m}$)	n	m
7.70	0.3	114	36°	395	0	1E−18	2.10	−0.5
				1,625	0.2			

Table 8 Calibrated material model parameters for BPP simulation

E (GPa)	Drucker–Prager plastic			Cap hardening		Creep consolidation		
	ν	d (MPa)	β	$p_{b(1\&2)}$ (MPa)	ε_v^{pl}	A ($Pa^{-n}s^{-m}$)	n	m
10.2	0.3	123	40°	430	0	1E−18	2.10	−0.5
				1,660	0.2			

Table 9 Anisotropy ratios $K_{(\cdot)}$ for anisotropic material model parameters, as determined through calibration of simulations with laboratory measurements separately for BPN and BPP 3 μm deep indentations

K_E	Drucker–Prager/Cap		
	K_d	K_β	$K_{p_{b(1)}}$
1.32	1.08	1.11	1.09

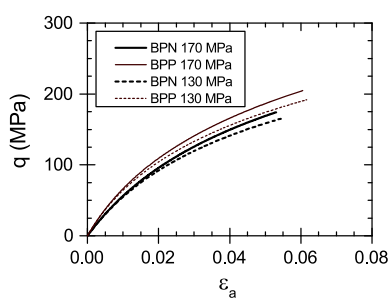

Fig. 10 Simulated triaxial compression results at various confining pressures for BPN (*dashed line*) and BPP (*solid line*) material parameters calibrated from BPN and BPP indentation measurements, respectively

ratios fall close to and between those determined from the measurements (Table 6), being greater than that of the relative plastic work $K_{W_p^*}$ and less than that of the hardness K_H.

In order to highlight the difference between the BPN and BPP calibrated material model parameters, hypothetical triaxial compression tests were simulated with both sets of calibrated parameters. These triaxial test simulations were run without creep, but with the same elastic and Drucker–Prager/Cap plasticity material parameters that were calibrated to the nanoindentation tests. They were run as

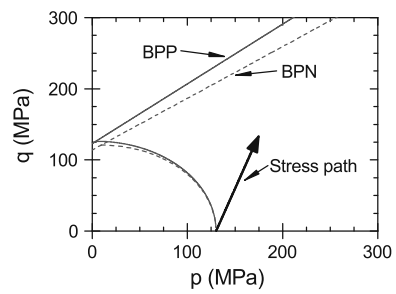

Fig. 11 Drucker–Prager/Cap yield surfaces for both BPN (*dashed line*) and BPP (*solid line*) calibrated material model parameters. Triaxial compression stress path shown for normally consolidated 130 MPa confining pressure

'normally consolidated', i.e., the initial stress point lies on the compression cap, at confining pressures of 130 and 170 MPa. The triaxial test simulation results are presented in Fig. 10 plotting the deviator stress $q = \sigma_1 - \sigma_3$, where σ_1 and σ_3 are, respectively, the major and minor principal stresses, versus axial strain ε_a. Figure 11 plots the two different yield surfaces, calibrated from BPN and BPP simulations, with the normally consolidated stress path of the 130 MPa confining pressure triaxial compression test shown. Clearly, the stress and strain fields developed under nanoindentation are complex, and indentation tests performed in BPN and BPP directions cannot be said to necessarily correspond to triaxial tests conducted on shale specimens with the major principal stress σ_1 oriented along BPN and BPP axes. However, we maintain that it is not unreasonable to take BPN and BPP nanoindentation experiments as being representative of the degree of anisotropy exhibited by the shale at this scale (as we have quantified with the anisotropy ratios $K_{(\cdot)}$). The differences then, between simulated triaxial compression tests using the BPN and BPP calibrated material model parameters as

shown in Fig. 9, provide an idea as to how much a triaxial specimen of this shale would be expected to vary in its stress–strain response under different orientations ranging from BPN and BPP orientations with respect to σ_1.

6 Summary and conclusions

Nanoindentation tests as shallow as 200 nm have provided in situ mechanical property measurements of the constituent materials comprising a highly heterogeneous sample of Woodford shale, whereas indentations ranging to depths of up to 5 μm have provided measurements of their composite mechanical properties. FIB–SEM imaging provided verification that indents at all length scales fell on sufficiently smooth regions and, along with EDX spectroscopy, provided for identification of the material phases on which the indents fell.

The FIB–SEM imaging further enabled the development of a mechanistic conceptual model describing the scale with respect to material heterogeneity for the organic-rich shale specimen: The specimen was found to be best described as being comprised of near micrometer sized particles of clay and other silicate minerals embedded in a mixed organic/clay matrix. Together with the nanoindentation testing, the FIB–SEM imaging identified a separation of scale at approximately 1 μm occurring between relatively homogeneous regions comprised of a single material phase and highly heterogeneous regions representing the composite material. By adopting a deterministic approach to verifying local surface smoothness independently for each indent, very shallow nanoindentation measurements engaging sub-micrometer constituent material particles were able to be made. These 200 nm deep indents were observed to be predominantly representative of the constituent phases on which they fell, whereas indents ranging from depths of 3 to 5 μm were shown to be representative of the composite (heterogeneous) material response. Indentations to depths of 1 μm were able to measure the mechanical properties of the supporting organic/clay matrix.

Nanoindentation testing was performed in both the bedding plane normal (BPN) and bedding plane perpendicular (BPP) directions to evaluate material anisotropy. Anisotropy of measured stiffness was found to be most pronounced in the organic/clay matrix, being stronger and stiffer in the BPP direction; however, indentations into $\geq$1 μm size clay particles exhibited significant anisotropy of this phase, being also stiffer in the BPP direction, but with greater hardness measured in the BPN direction. The larger of the indents measured significant anisotropy of the microscale heterogeneous shale material as well, being about 30 % stiffer with about 10–15 % greater hardness in the BPP direction.

A FE model of the nanoindentation experiments was developed and implemented with Drucker–Prager/Cap plasticity and consolidation creep. Plastic material parameters were calibrated to the 3 μm deep indentation measurements which represent the microscale stress–strain behavior of the heterogeneous shale. The calibrated simulations provide a means of extracting plastic material parameters from the nanoindentation experiments and also provide a means of further evaluating the plastic anisotropy exhibited by the shale. Simulations of triaxial compression tests conducted with the BPN and BPP calibrated material parameters highlight the anisotropic behavior of the shale, showing the disparity between BPN and BPP calibrated material parameters in the ductile stress–strain response. These FE simulations, conducted with a well-established isotropic material model, are further intended to inform and motivate presently ongoing research efforts to develop an appropriate finite strain anisotropic material model for shale at the nanoscale to microscale based on the experimental observations presented here, as well as ongoing experimental investigations into the nanoscale to microscale deformation mechanisms behind the observed anisotropic stress–strain behavior.

Acknowledgments This material is based upon work supported by the U.S. Department of Energy, Office of Science, Office of Basic Energy Sciences, Geosciences Research Program, under Award Number DE-FG02-03ER15454. L.A.B. and W.D.N. gratefully acknowledge support from the Office of Science, Office of Basic Energy Sciences, of the U.S. Department of Energy under Contract No. DE-FG02-04ER46163. Part of this work was performed at the Stanford Nano Shared Facilities, and the authors are grateful for their training and support. The first author is grateful for support from the Department of Defense (DoD) through the National Defense Science & Engineering Graduate Fellowship (NDSEG) Program. The authors wish to thank Dr. Younane N. Abousleiman of the University of Oklahoma for providing samples of Woodford shale, and Dr. Cindy Ross of Stanford's Department of Energy Resource Engineering for assistance in preparing the samples.

References

1. Abaqus (2011) Abaqus documentation. Technical report, Dassault Systems, Providence, RI, USA
2. Abousleiman YN, Hoang SK, Liu C (2014) Anisotropic porothermoelastic solution and hydro-thermal effects on fracture width in hydraulic fracturing. Int J Numer Anal Methods Geomech 38(5):493–517
3. Abousleiman Y, Tran M, Hoang S, Bobko C, Ortega A, Ulm F (2007) Geomechanics field characterization of Woodford shale: the next gas play. In: Proceedings—SPE annual technical conference and exhibition, Anaheim, CA, USA, pp 2127–2140
4. Arson C, Pereira JM (2013) Influence of damage on pore size distribution and permeability of rocks. Int J Numer Anal Methods Geomech 37(8):810–831

5. Barthélémy JF, Souque C, Daniel JM (2013) Nonlinear homogenization approach to the friction coefficient of a quartz-clay fault gouge. Int J Numer Anal Methods Geomech 37(13):1948–1968
6. Bennett R, O'Brien N, Hulbert M (1991) Determinants of clay and shale microfabric signatures: processes and mechanisms. In: Bennett R, Bryant W, Hulbert M (eds) Microstructure of fine-grained sediments: from Mud to Shale. Springer, New York
7. Boggs S (2009) Petrology of sedimentary rocks. Cambridge University Press, Cambridge
8. Bornert M, Vales F, Gharbi H, Minh D (2010) Multiscale full-field strain measurements for micromechanical investigations of the hydromechanical behavior of clayey rocks. Strain 46:33–46
9. Brooks Z, Ulm FJ, Einstein HH (2013) Environmental scanning electron microscopy (ESEM) and nanoindentation investigation of the crack tip process zone in marble. Acta Geotech 8(3):223–245
10. Cardott BJ (2012) Thermal maturity of Woodford Shale gas and oil plays, Oklahoma, USA. Int J Coal Geol 103:109–119
11. Curtis M, Ambrose R, Sondergeld CH, Rai C (2011) Transmission and scanning electron microscopy investigation of pore connectivity of gas shales on the nanoscale. In: SPE North American unconventional gas conference and exhibition, Woodlands, TX
12. Day-Stirrat R, Dutton S, Millken K, Loucks R, Aplin A, Hillier S, van der Pluijm B (2010) Fabric anisotropy induced by primary depositional variations in the silt: clay ratio in two fine-grained slope fan complexes: Texas gulf coast and northern north sea. Sediment Geol 226:42–53
13. Deirieh A, Ortega JA, Ulm FJ, Abousleiman Y (2012) Nanochemomechanical assessment of shale: a coupled WDS-indentation analysis. Acta Geotech 7(4):271–295
14. Dewers T, Heath J, Ewy R, Duranti L (2012) Three-dimensional pore networks and transport properties of a shale gas formation determined from focused ion beam serial imaging. Int J Oil Gas Coal Technol 5(2–3):229–248
15. Ewy RT (2014) Shale swelling/shrinkage and water content change due to imposed suction and due to direct brine contact. Acta Geotech 9:869–886
16. Foster CD, Mohammad Nejad T (2013) Embedded discontinuity finite element modeling of fluid flow in fractured porous media. Acta Geotech 8(1):49–57
17. Fu P, Johnson SM, Carrigan CR (2013) An explicitly coupled hydro-geomechanical model for simulating hydraulic fracturing in arbitrary discrete fracture networks. Int J Numer Anal Methods Geomech 37(14):2278–2300
18. Hall MR, Mooney SJ, Sturrock C, Matelloni P, Rigby SP (2013) An approach to characterisation of multi-scale pore geometry and correlation with moisture storage and transport coefficients in cement-stabilised soils. Acta Geotech 8(1):67–79
19. Hay J, Sondergeld CH (2010) Mechanical testing of shale by instrumented nanoindentation. Agilent Technologies App Note 5990-5816EN 1-8
20. He Z, Caratini G, Dormieux L, Kondo D (2013) Homogenization of anisotropic elastoplastic behaviors of a porous polycrystal with interface effects. Int J Numer Anal Methods Geomech 37(18):3213–3236
21. Hiller S (2006) Appendix a. Mineralogical and chemical data. Geological Society, London, Engineering Geology Special Publications, vol 21, pp 449–459
22. Hu DW, Zhou H, Shao JF (2013) An anisotropic damage-plasticity model for saturated quasi-brittle materials. Int J Numer Anal Meth Geomech 37(12):1691–1710
23. Hu DW, Zhang F, Shao JF (2014) Experimental study of poromechanical behavior of saturated claystone under triaxial compression. Acta Geotech 9(2):207–214
24. Ingram R (1953) Fissility of mudrocks. Geol Soc Am Bull 64:869–878
25. ISO-14577 (2002) Metallic materials—instrumented indentation test for hardness and materials parameters
26. Karim MR, Oka F, Krabbenhoft K, Leroueil S, Kimoto S (2013) Simulation of long-term consolidation behavior of soft sensitive clay using an elasto-viscoplastic constitutive model. Int J Numer Anal Methods Geomech 37(16):2801–2824
27. Kohli A, Zoback M (1983) Frictional properties of shale reservoir rocks. J Geophys Res Solid Earth 118:1–17
28. Kumar V (2012) Geomechanical characterization of shale using nano-indentation. Ph.D. thesis, OK University
29. Lee S, Hyder L, Alley P (1991) Microstructural and mineralogical characterization of selected shales in support of nuclear waste repository studies. In: Bennett R, Bryant W, Hulbert M (eds) Microstructure of fine-grained sediments: from Mud to Shale. Springer, New York, NY
30. Liu F, Borja RI (2013) Extended finite element framework for fault rupture dynamics including bulk plasticity. Int J Numer Anal Methods Geomech 37(18):3087–3111
31. Lonardelli I, Wenk H, Ren Y (2007) Preferred orientation and elastic anisotropy in shales. Geophysics 72(2):D33–D40
32. Lucas B, Oliver W, Swindeman J (1998) The dynamics of frequency-specific, depth-sensing indentation testing. In: In: Materials research society symposium proceedings vol 522, pp 3–14
33. Nedjar B, Le Roy R (2013) An approach to the modeling of viscoelastic damage. Application to the long-term creep of gypsum rock materials. Int J Numer Anal Methods Geomech 37(9):1066–1078
34. Pettijohn F (1975) Sedimentary rocks, 3rd edn. Harper and Row Publishers, New York, NY
35. Pietruszczak S, Guo P (2013) Description of deformation process in inherently anisotropic granular materials. Int J Numer Anal Methods Geomech 37(5):478–490
36. Powell J, Take W, Siemens G, Remenda V (2012) Time-dependent behavior of the Bearpaw Shale on oedometric loading and unloading. Can Geotech J 49:427–441
37. Salager S, Francois B, Nuth M, Laloui L (2013) Constitutive analysis of the mechanical anisotropy of Opalinus clay. Acta Geotech 8(2):137–154
38. Schaedlich B, Schweiger HF (2013) A multilaminate constitutive model accounting for anisotropic small strain stiffness. Int J Numer Anal Methods Geomech 37(10):1337–1362
39. Shaw D, Weaver C (1965) The mineralogical composition of shales. J Sediment Pet 35(1):213–222
40. Shim S, Oliver WC, Pharr GM (2005) A critical examination of the Berkovich vs. conical indentation based on 3D finite element calculation. In: Materials research society symposium proceedings vol 841, pp 39–43
41. Sondergeld C, Ambrose R, Rai C, Moncrieff J (2010) Microstructural studies of gas shales. In: Proceedings of SPE unconventional gas conference, Pittsburgh, PA, USA
42. Sarris E, Papanastasiou P (2013) Numerical modeling of fluid-driven fractures in cohesive poroelastoplastic continuum. Int J Numer Anal Methods Geomech 37(12):1822–1846
43. Sone H, Zoback M (2013) Mechanical properties of shale-gas reservoir rocks—part 2: ductile creep, brittle strength, and their relation to the elastic modulus. Can Geotech J 78:D393–D402
44. Tian H, Xu T, Wang F, Patil VV, Sun Y, Yue G (2014) A numerical study of mineral alteration and self-sealing efficiency of a caprock for CO_2 geological storage. Acta Geotech 9(1):87–100
45. Tran HTT, Wong H, Dubujet P, Doanh T (2014) Simulating the effects of induced anisotropy on liquefaction potential using a new constitutive model. Int J Numer Anal Methods Geomech 38(10):1013–1035
46. Ulm F, Aboussleiman Y (2006) The nanogranular nature of shale. Acta Geotech 1(2):77–88

47. Valcke S, Casey M, Lloyd G, Kendall J, Fisher Q (2006) Lattice preferred orientation and seismic anisotropy in sedimentary rocks. Geopys J Int 166:652–666
48. Vallin V, Pereira JM, Fabbri A, Wong H (2013) Numerical modelling of the hydro-chemo-mechanical behaviour of geomaterials in the context of CO_2 injection. Int J Numer Anal Methods Geomech 37(17):3052–3069
49. Vernik L, Nur A (1992) Ultrasonic velocity and anisotropy of hydrocarbon source rocks. Geophysics 57(5):727–735
50. Vitone C, Viggiani G, Cotecchia F, Hall SA (2013b) Localized deformation in intensely fissured clays studied by 2D digital image correlation. Acta Geotech 8(3):247–263
51. Vu MN, Pouya A, Seyedi DM (2014) Theoretical and numerical study of the steady-state flow through finite fractured porous media. Int J Numer Anal Methods Geomech 38(3):221–235
52. White JA (2014) Anisotropic damage of rock joints during cyclic loading: constitutive framework and numerical integration. Int J Numer Anal Methods Geomech 38(10):1036–1057
53. Xie H, Li X, Fang Z, Wang Y, Li Q, Shi L, Bai B, Wei N, Hou Z (2014) Carbon geological utilization and storage in China: current status and perspectives. Acta Geotech 9(1):7–27
54. Yin ZY, Xu Q, Hicher PY (2013b) A simple critical-state-based double-yield-surface model for clay behavior under complex loading. Acta Geotech 8(5):509–523
55. Zheng P, Ding B, Zhang W, Zhao SX, Zhu Y (2014) Dynamic response to fluid extraction from a poroelastic half-space. Int J Numer Anal Methods Geomech 38(7):661–678